Absolute differential and total cross sections for direct and charge-transfer scattering of keV protons by O_2

R. Cabrera-Trujillo, Y. Öhrn, E. Deumens, and J. R. Sabin
Quantum Theory Project, Departments of Physics and Chemistry, University of Florida, P.O. Box 118435, Gainesville, Florida 32611-8435, USA

B. G. Lindsay
Department of Physics and Astronomy, Rice University, 6100 Main Street, Houston, Texas 77005-1892, USA
(Received 12 April 2004; revised manuscript received 8 June 2004; published 12 October 2004)

Calculated and experimental differential direct, charge-transfer, and total scattering cross sections are presented for collisions of H^+ with O_2. Experimental cross sections are obtained for projectile energies of 0.5, 1.5, and 5.0 keV, and scattering angles of 0.15° to 5° while the theoretical results extend from 0.5 to 25 keV and encompass scattering angles from 0.01° to 180°. We find good agreement between the calculated and measured differential and total cross sections. Also, a diffraction slit effect, which is target orientation dependent, is found in the differential scattering cross section. A theoretical explanation of the effect is presented.

DOI: 10.1103/PhysRevA.70.042705 PACS number(s): 34.50.−s, 34.70.+e

I. INTRODUCTION

Atomic and molecular collision processes are of fundamental physical interest and play key roles in many diverse fields of study. Angular scattering of ions by atoms and molecules may be used to examine the basic interactions, the scattering potentials, and the dynamical properties of the interacting system. The two processes of interest here are direct scattering and charge transfer (or electron capture) resulting in the transfer of one electron to the projectile. A complete description of the ion-molecule collision system requires that the dynamics of both the electrons and the nuclei be accounted for, and therefore both must be incorporated into the theoretical scattering model. The system chosen for study here, H^+ colliding with O_2, extends and complements our previous studies of H^+ with N_2 [1] and H^+ with H_2 [2].

Molecular oxygen, and atomic oxygen which results from dissociation of O_2 by solar radiation, are two of the main constituents of the Earth's atmosphere and interaction often occurs with protons that arrive in the solar wind as a result of solar flares. Typical proton kinetic energies are in the keV range; thus ionization and charge exchange processes may significantly influence the dynamics of the upper atmosphere. These interactions are particularly relevant to terrestrial auroral precipitation models [3]. There is also some interest in the atmospheres of planets where the absence of a magnetic field allows more direct solar wind bombardment than on Earth [4]. Furthermore, knowledge of the $H^+ \rightarrow O_2$ cross sections has sometimes been an important component of related laboratory studies [3,5].

Previous experimental and theoretical studies have tended to focus on the atmospherically important process of electron capture by atomic oxygen [3,6–10]. By contrast, no prior measurements or calculations are available for the direct scattering of H^+ by O_2, and few measurement are available for the charge exchange process [3,11–13].

In this work we present calculations and experimental measurements of the absolute direct and charge transfer scattering cross sections for protons colliding with molecular oxygen. In the following section, Sec. II, we provide a summary of the electron-nuclear dynamics (END) model used in this work and its implementation to calculate direct and charge transfer cross sections. The END model, which was developed here [14], incorporates the dynamics of the electrons and the nuclei. In Sec. III we present details of the experimental arrangement. Section IV shows our theoretical and experimental results. Finally, in Sec. V, we present our conclusions.

II. THEORETICAL SURVEY

A. Electron-nuclear dynamics

Our approach for analysis of the scattering processes is based on the application of the time-dependent variational principle (TDVP) to the Schrödinger equation [15], where the wave function is described in a coherent state representation. As the details of the END method have been reported elsewhere [14,16,17], we present here a summary of the theory.

We use a parametrization of the wave function in a coherent state manifold, which leads to a system of Hamilton's equations of motion [14]. The variational wave function $|\xi\rangle$ is a molecular coherent state written in terms of the coupled electronic and nuclear wave functions, respectively.

The simplest level of the END approach employs a single spin unrestricted electronic determinant. Each spin orbital is expressed in terms of a basis of atomic Gaussian type orbitals of rank K with complex coefficients $\{z_{ji}\}$. The Gaussian type orbitals are centered on the average positions **R** of the participating atomic nuclei, which are moving with momentum **P**. This representation takes into account the momentum of the electron explicitly through the use of electron translation factors (ETF) [18]. The particular form of parametrization of the wave function with complex, time dependent coefficients, z_{ji}, is due to Thouless [19], and is an example of so-called generalized coherent states [20].

The nuclear part of the wave function is represented by localized Gaussians, or, in the narrow wave-packet limit by classical trajectories.

Application of the TDVP then yields the dynamical equations [14]. Solving the set of dynamical equations for $\{\mathbf{z},\mathbf{R},\mathbf{P}\}$ as a function of the time, t, yields the evolving molecular state that describes the processes that take place during the collision. For the purpose of discussing charge exchange, we make use of the Mulliken population analysis [21,22] for the projectile or target (see Secs. II C and IV D).

The END method has been implemented in the ENDyne program package [23].

B. Direct differential cross section

Since the simplest level of END is based on the narrow width limit of the nuclear wave packets, it requires semiclassical corrections for the scattering process. We have implemented [24] the Schiff approximation [25] which takes into account the quantum effects of nuclei scattering.

In this description, the deflection function [the angle between the incoming beam and the scattered particle $\Theta(b)$] becomes the signature of the projectile-target collision and determines the shape of the differential cross section through the scattering amplitude $f(\theta,E_p)$. In time-independent theory, the deflection function is related to the collision phase-shift, which in turn is related to the static scattering potential. In the END model, since there is a time-dependent process and all the collision channels are unrestricted, the deflection function describes a realistic dynamical potential.

For a detailed review of the Schiff approximation, its extension, and implementation, see Ref. [24].

C. Charge transfer differential cross section

At the end of the dynamics, we determine the total electron charge density of the system. The Mulliken analysis [21,22] allows us to determine the probability for electrons to be associated with each of basis function for each atomic nucleus.

In the linear combination of atomic orbitals method for electronic structure, each electron of the system is described by a spin orbital as the sum over atomic basis orbitals. Integration of the total electron charge density over all space yields the number of electrons as a sum over the electron population of each atom. From the electrons associated with an atom, and the initial number of electrons, one determines the electron capture (or loss) probability $P_{\mathrm{exch}}(b,E_p)$ [22].

D. Details of calculations

For the time-dependent analysis of the collision, the END approach requires the specification of initial conditions of the system under consideration. In Fig. 1, we show a schematic representation of the projectile-target arrangement. The initial projectile velocity is set parallel to the z axis and directed towards the stationary target with an impact parameter, b. In the case of atomic projectiles, as in this case, we need to consider only the initial orientations of the target. The target center of mass is initially placed at the origin of a Cartesian laboratory coordinate system and its orientation is specified by the angles α and β.

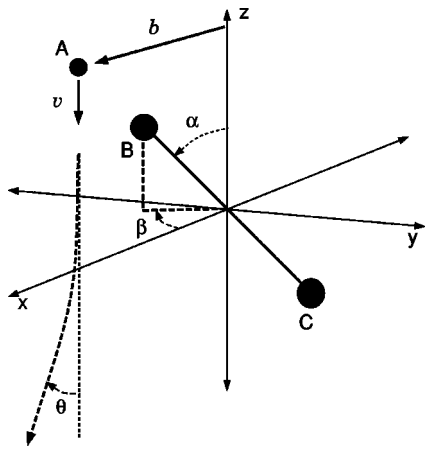

FIG. 1. Schematic representation of the initial conditions of the projectile-target system as required by the END formalism.

We have constructed the numerical grid for the target orientation with increments of $\Delta\alpha=\Delta\beta=45°=\pi/4$, thus requiring nine symmetry independent target orientations (see Sec. IV B). We label those orientation by the pair (α,β), e.g., the orientation with the projectile beam parallel to the molecular bond is (0,0). The orientational average is conducted as described in Ref. [26].

The molecular target is initially in its electronic ground state, ${}^3\Sigma_g^-$, and at the equilibrium geometry as computed in the computational basis at the SCF level. The basis functions used for the atomic orbital expansion are derived from those optimized by Dunning [27,28]. For the hydrogen atomic structure (projectile), the basis set consists of $[5s2p/5s2p]$ with the addition of an even-tempered diffuse s and p orbital for a better description of the long range interaction. For the oxygen atomic structure, we use a $[6s3p/3s2p]$ basis set.

We consider values of the impact parameter from 0.0 to 15.0 a.u. which we separate into three regions. For close collisions, from 0.0 to 6.0 a.u., we use steps of 0.1 a.u. For the intermediate region, from 6.0 to 10.0 a.u., we use steps of 0.5 a.u., and for $b>10.0$, we use steps of 1.0. This gives us 74 fully dynamical END trajectories for each target orientation and projectile energy. Larger impact parameters do not contribute to the computed observables, since most of the dynamics occurs in the close interaction region ($b<10$ a.u.) as observed in Fig. 2. Note that, for high energies, the dynamics requires a larger number of excited states, thus making our results at 25 keV a good test for the numerical calculation.

The projectile starts 20 a.u. from the target, and the trajectory is evolved until the projectile is 20 a.u. past the target, or until there are no longer changes in the energy, velocity, or charge of the projectile. This is the closest distance we can put the projectile, and still warrant stability of the results. By placing the projectile at larger distances nothing is gained as observed in Fig. 3, where we placed the projectile at 30 a.u. from the target and compared the results to the trajectory when the projectile is placed at 20 a.u. (dashed line) observing that both results overlap. The numerical difference

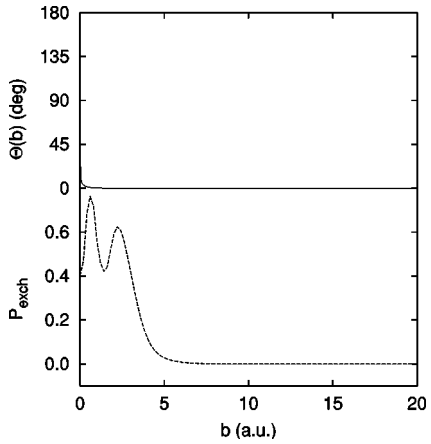

FIG. 2. Deflection function, $\Theta(b)$, and charge exchange probability, P_{exch}, as a function of the impact parameter, b, for a projectile energy of 25 keV. There is no significant contribution to the observables for $b>10$ a.u., thus $0<b<15$ a.u. is a sufficient impact parameter range to perform the calculations.

in the observables is less that 10^{-5}%, being within the numerical precision of the calculations. Thus, at the end of each trajectory, one obtains the total wave function, the nuclear positions and momenta, and therefore, one is able to calculate the deflection function, $\Theta(b)$, and electronic properties, e.g., charge transfer and energy loss, as well as rovibrational properties of molecular products when of interest.

III. EXPERIMENTAL APPROACH

The apparatus employed for both the charge transfer and direct scattering measurements is shown schematically in Fig. 4. The apparatus and the techniques used have been described in detail previously [3,11,29], and are only discussed briefly here. Ions are extracted from a low-pressure plasma-type ion source containing H_2, accelerated to the desired energy, and focused by an electrostatic lens. Two con-

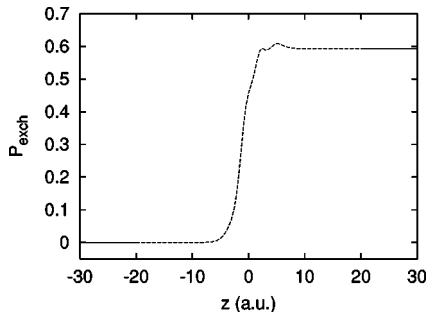

FIG. 3. Charge exchange probability for H^+ colliding with O_2 at 25 keV as a function of the z component of the projectile position. The trajectory is for an impact parameter $b=2.5$ a.u. and shows the results of two different initial distances of the projectile from the target: 20 a.u. (dashed line) and 30 a.u. (solid line). Note that the two lines overlap showing stability of the computed observables for longer time dynamics and that the final exchange probability is within the same numerical precision when starting at 20 a.u. as when starting at 30 a.u.

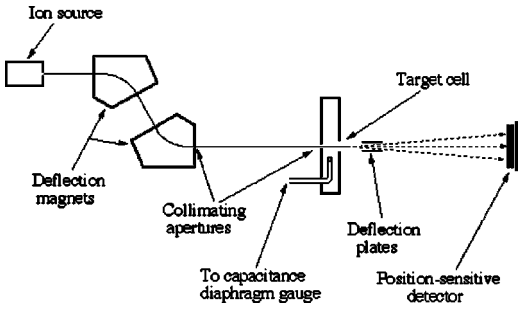

FIG. 4. Schematics of the scattering apparatus.

focal 60° sector magnets are used to select ions of the desired mass-to-charge ratio. Ions passing through a pair of laser drilled apertures form a beam with an angular divergence of approximately 0.02°. This collimated proton beam passes through a short target cell and impacts a position-sensitive detector (PSD) [30], located 26 cm beyond the target cell. The PSD serves to measure the flux of ions passing through the target cell and to measure the flux and positions of impact of scattered product species. An electric field established between a pair of deflection plates located between the target cell and the PSD is used to prevent ions from striking the PSD when required.

In order to measure the differential charge-transfer cross section, O_2 is admitted to the target cell, and the angles of scatter of the neutral H atoms, formed by charge transfer of the primary H^+ ions, are determined from their positions of impact on the PSD. Unscattered primary H^+ ions are normally deflected away from the PSD, but are allowed to impact it periodically to assess the primary beam flux. These measurements, together with knowledge of the target number density (obtained using a capacitance diaphragm absolute pressure gauge [31]) and the target length are sufficient to determine the DCS via the following equation:

$$\frac{d\sigma(\theta)}{d\Omega} = \frac{\Delta S(\theta)}{Snl\Delta\Omega}, \tag{1}$$

where S is the primary ion beam flux, ΔS is the neutral flux scattered at angle θ into a solid angle $\Delta\Omega$, n is the target number density, and l is the target cell length.

A full account of the procedure for determining direct scattering differential cross sections has been given by Newman *et al.* [32]. In this case, both the primary beam and scattered product species are allowed to impact the PSD. Essentially, the primary beam flux S is the total flux of particles impacting the detector, while $\Delta S(\theta)$ is the H^+ ion flux scattered at angle θ into a solid angle $\Delta\Omega$ and the absolute cross section is again defined by Eq. (1). Determination of the scattered ion flux is complicated by the fact that, in addition to the primary and scattered H^+ ions, fast neutral H charge transfer products are also detected. It is therefore necessary to conduct an additional measurement to assess the number of H atoms produced and subtract this H-atom signal from the total scattering signal to arrive at the scattered H^+ signal. As the charge transfer and direct scattering cross sections are comparable, this procedure renders the H^+ direct scattering cross section more susceptible to systematic errors

TABLE I. Glory and rainbow angle for $H^+ \rightarrow O_2$ as a function of the projectile energy for the three minimal target orientations (0,0), (90,0), and (90,90). The impact parameter is in a.u. and the angle is in degrees.

	Glory angle $\Theta_g(b_g)=0$			Rainbow angle $\Theta_r(b_r)$		
$E_p \backslash (\alpha,\beta)$	(0,0)	(90,0)	(90,90)	(0,0)	(90,0)	(90,90)
500 eV	1.79	2.77	0.0, 2.52	$\Theta_r(2.60)=0.80$	$\Theta_r(3.48)=0.63$	$\Theta_r(0.59)=2.20$, $\Theta_r(3.17)=0.16$
1.5 keV	1.82	2.79	0.0, 3.23	$\Theta_r(2.36)=0.17$	$\Theta_r(3.48)=0.18$	$\Theta_r(0.61)=0.79$, $\Theta_r(4.09)=0.03$
5.0 keV	2.67	2.97	0.0, 2.84	$\Theta_r(3.52)=0.03$	$\Theta_r(3.92)=0.04$	$\Theta_r(0.64)=0.26$, $\Theta_r(3.51)=0.010$
10.0 keV	2.66	3.12	0.0, 2.48	$\Theta_r(3.27)=0.01$	$\Theta_r(3.94)=0.02$	$\Theta_r(0.61)=0.13$, $\Theta_r(3.07)=0.006$
25.0 keV	2.40	3.06	0.0, 2.24	$\Theta_r(2.93)=0.004$	$\Theta_r(3.72)=0.01$	$\Theta_r(0.54)=0.05$, $\Theta_r(2.74)=0.001$

resulting in larger overall uncertainties than for the charge transfer measurements.

IV. RESULTS

A. Deflection function

The projectile scattering angle, θ, is determined from the final and initial projectile momenta $\mathbf{P}_p^f$ and $\mathbf{P}_p^i$, respectively. This also defines the deflection function $\Theta(b)$. For a positive defection function, the projectile is repelled by the target. For a negative angle, the projectile is attracted. In a plot of the deflection function as a function of the impact parameter, one observes that the curve can cross $\Theta=0$ for some given impact parameters. This is the glory angle where classically the differential cross section diverges. Furthermore, the deflection function can show a maximum (or minimum) with zero slope in the attractive (or repulsive) region. This defines the so-called rainbow angles. Since we have several initial target orientations, we may encounter rainbow and glory angles for each of them. There we can use a semiclassical model, e.g., the Airy approximation, Uniform approximation, etc. [33] if required. In this work, we use the Schiff approximation as it includes all the terms of the Born series and treats the rainbow and glory angles in a single approach without requiring separation into different scattering regions.

In Table I we present the glory and rainbow angles as a function of the impact parameter for the three minimal target orientations and projectile energy as obtained from the END trajectories. The minimal three target orientations are (0,0), (90,0), and (90,90), which locate the molecular bond along the three main axis in a Cartesian frame. Later, we discuss the effects on the differential cross section of this coarse orientational grid. From the results of Table I, we note that the glory impact parameter has a maximum around $E_p \sim 5.0$ keV for all three orientations. For the rainbow impact parameter, a similar behavior is observed. Furthermore, the value of the rainbow angle increases as the projectile energy decreases.

B. Direct differential cross section

From the deflection function, we obtain the phase shift as needed by the Schiff approximation [24,25] to calculate the direct differential cross section.

Figure 5 shows the calculated absolute direct differential cross section for $H^+ \rightarrow O_2$, for scattering angles from 0.01° to 180° and for projectile energies of 0.5, 1.5, 5.0, 10.0, and 25.0 keV averaged over all nine target orientations. In the

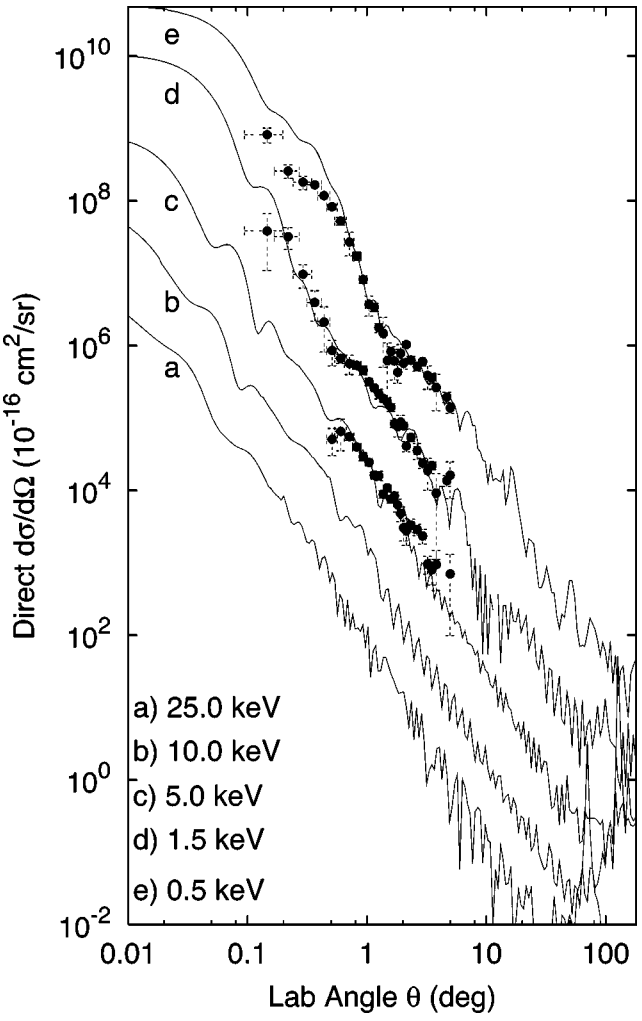

FIG. 5. Absolute direct differential cross section for protons colliding with molecular oxygen for projectile energies of 0.5, 1.5, 5.0, 10.0, and 25.0 keV. The lines represent our theoretical work and the solid circles with error bars are our experimental results. For clarity, the curves b, c, d, and e have been multiplied by 10, 10^2, 10^3, and 10^4, respectively.

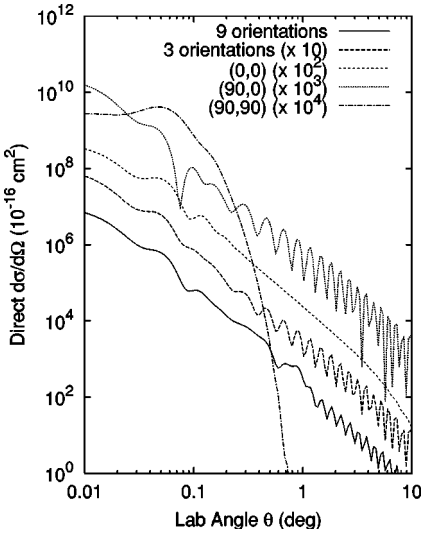

FIG. 6. Absolute direct differential cross section for protons colliding with molecular oxygen for the projectile energy of 10.0 keV for a three point orientational grid and a nine point orientational grid. The solid line is the result for the nine point grid. The dashed line is the three point orientational grid. Also we present the three individual contributions of the three point grid (note the scaled factor to avoid overlapping of the lines).

same figure we compare with our experimental results the energies of 0.5, 1.5, and 5.0 keV for the scattering angles from 0.15° to 5.0°. We note that the results of Fig. 5 use the Schiff approximation which provides the correct trend for calculated small scattering angle (forward peak character of the scattering). From the results shown in Table I, we note that for low projectile energies, the rainbow angle increases. That is observed in the structure of the differential cross section in Fig. 5, were a bump appears for lower energies and angles larger than Θ_r. The effect of the glory angle is observed in the correct form of the forward peak character of the differential cross section as $\theta \rightarrow 0$. For the 0.5 keV energy region (curve e), we note a small discrepancy for $0.1 < \theta < 0.8$ when comparing our experimental results to our calculated direct differential cross section. The reason for this is twofold. First, the single determinant description does not incorporate the multiconfigurational representation of the wave function that is needed to properly describe the dynamics of O_2 at low projectile energies (*vide infra*). Second, at lower energies, the projectile spends more time in the vicinity of the target, thus emphasizing orientational effects on the dynamics of the collision.

We note a uniform oscillatory structure in the theoretical results for high projectile energies that is not observed in the experimental data. By looking at the deflection function, we note that there are some orientations where the projectile penetrates the molecular bond. This scattering is observed in the differential cross section as a diffraction effect (slit effect due to the two atomic nuclei target, *vide infra*).

To see the effects of the orientational grid on our results, in Fig. 6 we present the direct differential cross section for the projectile energy of 10 keV for an orientational average grid of three minimal orientations ($\Delta\alpha = \Delta\beta = 90°$) and compare to the nine point orientational grid results. In the same

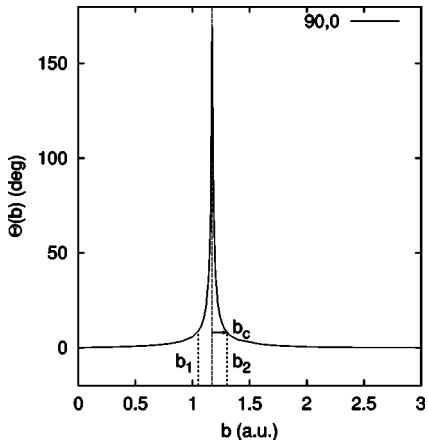

FIG. 7. Deflection function for H^+ colliding with O_2 at an energy of 10.0 keV and target orientation (90,0). The impact parameter b_1 lies within the molecular bond and the impact parameter b_2 is outside, both producing the same scattering angle θ. Thus the scattering from the O atom siting at 1.1711 a.u. (half the bond length) can be seen as a diffracting slit.

figure, we show the contribution of the individual orientations. We note that the oscillations are produced by the scattering along the orientation (90,0) (impact parameter running along the molecular bond) in agreement with the idea of a slit effect, while the other orientations have a smooth behavior as a function of the scattering angle. When the number of target orientations is increased, the oscillations are averaged out, which is observed in the experimental data. From the results in Fig. 5, we note that the average grid of nine points produces results within the experimental error, however, the oscillations are still present. Due to the high computational cost in increasing the grid from $\Delta\alpha = \Delta\beta = 45°$ to, e.g., $\Delta\alpha = \Delta\beta = 20°$ where we will have 164 target orientations, we consider that more than nine grid points is unnecessary and that for some systems even a three points grid produces acceptable results [2].

Diffraction slit effect

In order to provide an explanation of the slit effect, we refer to Fig. 7 where we plot the deflection function for orientation (90,0). Here the two trajectories at impact parameters b_1 and b_2 are scattered with the same scattering angle, thus arriving at the same point in the detector. The trajectory b_1 is scattered from inside the molecular bond while b_2 is scattered from the outside of the molecule.

The de Broglie wavelength of the projectile is $\lambda = 2\pi\hbar/p$, where p is the projectile momentum. Constructive interference from these two source points requires $n\lambda = (b_2^c - b_1^c)\sin\theta_c$, where θ_c is the scattering angle where there is a maximum (constructive interference) in the differential cross section. Similarly, for destructive interference $(n+1/2)\lambda = (b_2^d - b_1^d)\sin\theta_d$. From the symmetry of the collision around the atom at $D/2 = 1.1711$ a.u. (half the bond length) we note that $b_2 - b_1 \simeq 2b_c$. In order to find an analytical relation between the constructive and destructive scattering angles and the projectile velocity, we need an analytical form for the deflection function. Assuming, for simplicity, that the scatter-

ing is Coulombic, then $b(\theta)=Z_1Z_2e^2/2E_p\cot(\theta/2)$. Therefore

$$\frac{\lambda}{2}=2[b_c(\theta_c)\sin(\theta_c)-b_d(\theta_d)\sin(\theta_d)] \tag{2}$$

$$=\frac{Z_1Z_2e^2}{E_p}[\cos^2(\theta_c/2)-\cos^2(\theta_d/2)] \tag{3}$$

or, in terms of the projectile velocity,

$$v=Z_1Z_2v_0[\cos^2(\theta_c/2)-\cos^2(\theta_d/2)], \tag{4}$$

where $v_0=e^2/\hbar$ is the Bohr velocity. For small scattering angles ($\theta<10°$), we can approximate Eq. (4) by

$$v=Z_1Z_2v_0(\theta_c^2-\theta_d^2). \tag{5}$$

Thus the higher the projectile velocity, the more separated are the minima and the maxima (destructive and constructive interference) of the differential cross section. In a logarithmic plot, as is the usual case for the differential cross section, we have that $\theta\rightarrow e^{\theta}$, thus

$$\Delta\theta\simeq\frac{v}{2Z_1Z_2v_0\theta_c}, \tag{6}$$

where $\Delta\theta$ is the linear difference between the two constructive and destructive angles. From this, we note that, in the neighborhood of θ_c and for a given projectile energy, $\Delta\theta$ is almost constant, which is the behavior observed in Fig. 5. Also, the difference gets smaller for larger scattering angles and/or for a higher charge projectile or target. Note that for small scattering angles, the glory angle effect starts to dominate and the oscillations disappear for all the target orientations, as expected.

Although this analysis is obtained within the assumption of Coulombic scattering, the general trend is explained. That is, interference effects due to a slit effect produced by the diatomic molecule and the constant difference in phase for the constructive and destructive phase on a log scale plot of the differential cross section are reproduced. Of course, in the results presented in Fig. 5, the Schiff approximation has taken into account the interference from the theoretical deflection function obtained by the END approach. Furthermore, the effect just discussed is independent of the semiclassical model used to describe the differential cross section, since Eqs. (2)–(6) are just based on pure quantum wave interference. Also, when the result of each orientation is averaged over all the target orientations, the slit effects disappear, as is observed in our experimental results.

C. Charge exchange probability

As described in Sec. II C, we obtain the electron exchange probability by using the results of the Mulliken population analysis. To understand the behavior of the electron transfer process as a function of the projectile energy and impact parameter, we show in Fig. 8 the probability for electron capture for $H^+\rightarrow O_2$ times the impact parameter for orientation (0,0). The area under the curve for a fixed projectile energy is proportional to the total electron capture cross section [see Sec. IV E, Eq. (7)]. Furthermore, the plot shows that the interaction region where this process occurs with the highest probability is near $b=4$ for low energies, with b somewhat lower at larger E_p.

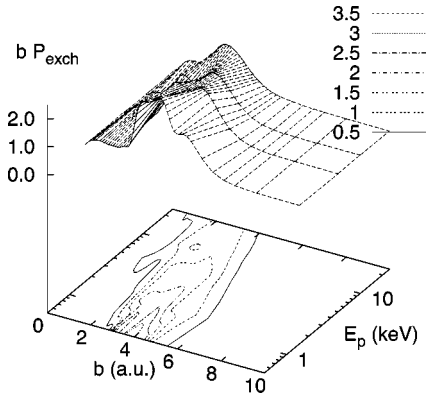

FIG. 8. Impact parameter times the probability for electron capture for $H^+\rightarrow O_2$ for the target orientation (0,0) as a function of the impact parameter and projectile energy.

For orientation (0,0), the large electron transfer probability occurs in the impact parameter region $1<b<5$ a.u. at high energies, where the p-like orbitals of O_2 have significant density. As the projectile energy decreases, the range in the impact parameter narrows, and therefore the total capture cross section for this orientation is reduced. The probability for electron capture resides mostly at $b\sim3$ and $b\sim5$ where the hydrogen 1s and 2s, 2p states are in resonance with the $2p\pi^*$ orbital of O_2.

In Fig. 9 we present a similar plot for orientation (90,0). In this case, since the projectile impact parameter runs over the O_2 bond length, the range for significant electron capture goes from $0<b<6$ a.u., with a large contribution from the outer region of the molecular bond for high projectile energies.

Finally, in Fig. 10, we show the projectile electron capture probability times the impact parameter for $H^+\rightarrow O_2$ for orientation (90,90). In this case, the exchange probability is larger and with a wider range of impact parameter, since in

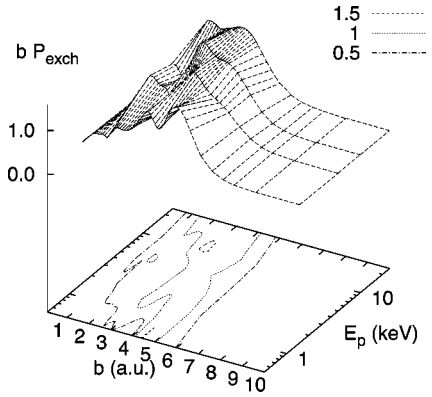

FIG. 9. Impact parameter times the probability for electron capture for $H^+\rightarrow O_2$ for the target orientation (90,0) as a function of the impact parameter and projectile energy.

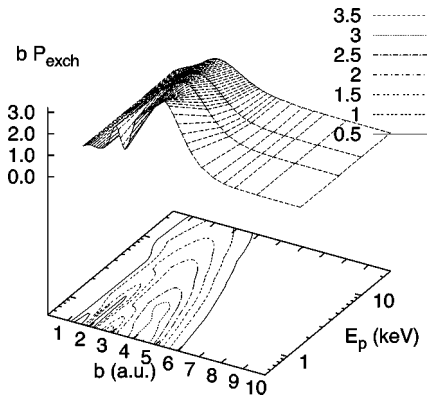

FIG. 10. Impact parameter times the probability for electron capture for $H^+ \rightarrow O_2$ for the target orientation (90,90) as a function of the impact parameter and projectile energy.

this orientation the projectile crosses the double bond made by the oxygen *p* orbitals. For low projectile energies, we note oscillations in the charge transfer, due to resonances among the projectile and target energy levels.

From the results of Figs. 8–10, we note that the charge exchange probability occurs for $b < 10$ a.u., in the so-called close interaction region, for all the projectile energies.

D. Charge transfer differential cross section

From the previous results, we can map the impact parameter onto the scattering angle by means of the deflection function. This allows us to obtain the exchange differential cross section (see Ref. [1] for more details of the procedure).

The calculated charge transfer differential cross sections for $H^+ \rightarrow O_2$ is shown in Fig. 11 for the same range of projectile energies as displayed in Fig. 5 and averaged over the nine target orientation grid. In the same figure, we present our experimental results (solid circles) as well as comparison to the data from Gao *et al.* [11] for the same set of projectile energies. As mentioned before, our theoretical results are based on the Mulliken population analysis and therefore do not include interference effects for the probability amplitude [1]. This is particularly observed in the low energy curves where the effects are more striking, and for the small scattering angles, where long range interactions are important.

For lower projectile energies quantum effects become important, as shown by the 0.5 keV curve. Furthermore, the description of the electronic structure of O_2 by a single determinant is too restrictive at low projectile energies where multiconfigurational effects in the electronic structure of O_2 are important. This is observed particularly at small scattering angles (large impact parameters) where the long range interaction of the electronic structure becomes important and a more detailed description of the electronic structure is suitable. At high energies, where the quantum interference effects are small, the agreement between theory and experiment is good. In general, the theoretical curves follow the trend of the experimental data, giving us confidence in the dynamical description for the electron transfer process presented here.

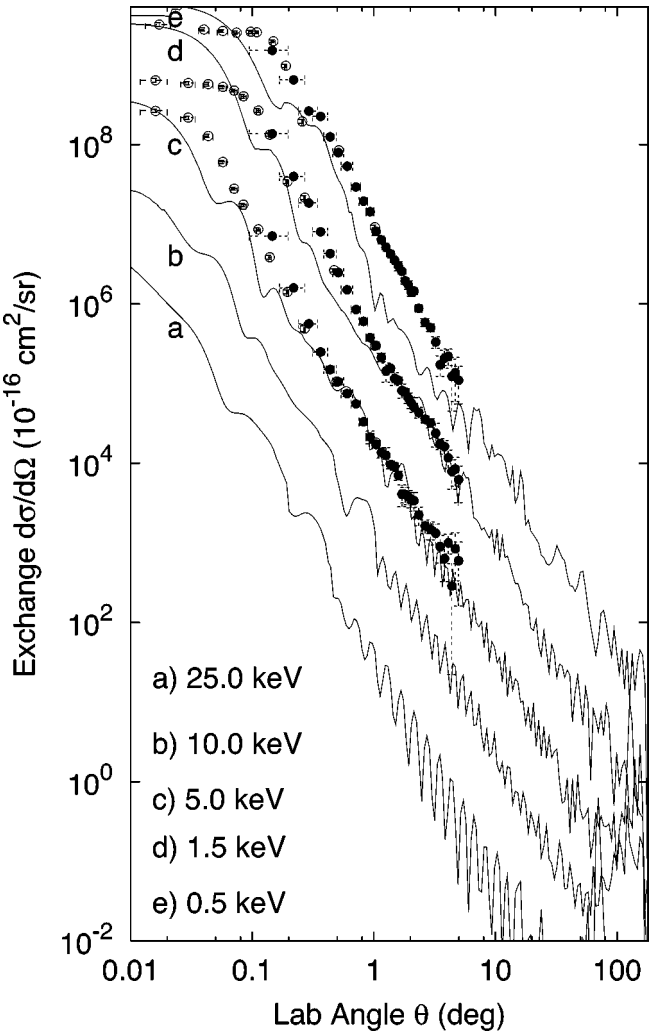

FIG. 11. Absolute exchange differential cross section for protons colliding with molecular oxygen for projectile energies of 0.5, 1.5, 5.0, 10.0, and 25.0 keV. The solid line represents our theoretical work; solid circles are our experimental results; and empty circles those of Gao *et al.* [11]. For clarity, the curves b, c, d, and e have been multiplied by 10, 10^2, 10^3, and 10^4, respectively.

E. Integral cross section

By integration of the exchange differential cross section over the scattering angle, or by mapping to the impact parameter by means of the deflection function, one obtains an integrated charge exchange total cross section, i.e.,

$$\sigma_{\text{exch}} = \int \frac{d\sigma_{\text{exch}}}{d\Omega} d\Omega \tag{7}$$

or

$$\sigma_{\text{exch}} = \int P_{\text{exch}} b db d\varphi. \tag{8}$$

Let us note that Eq. (8) does not include interference between different trajectories that result in scattering at the same angle, since it results from the assumption of a classical differential cross section. Thus the results of Eqs. (7) and (8)

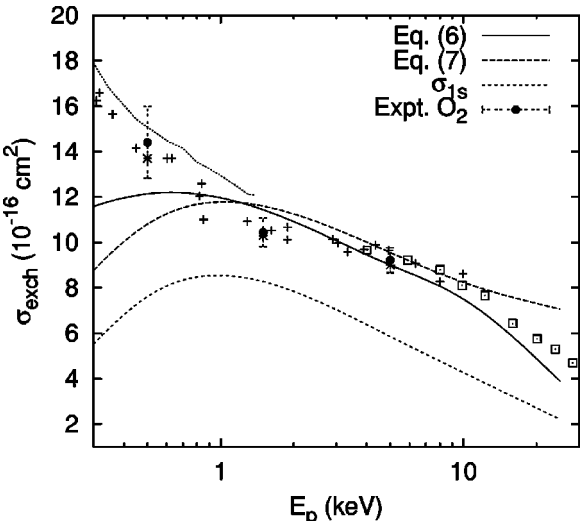

FIG. 12. Integral exchange cross section for protons colliding with molecular oxygen for projectile energies from 0.3 up to 25 keV. The theoretical total electron capture cross section from Eq. (7) is shown as a solid line and the result from Eq. (8) is shown as a dashed line. Our experimental results for the total cross section for O_2 are the solid circles with error bars. Previous experimental data are also shown: Lindsay *et al.* [3] (∗); Koopman [13] (dotted line); Stebbings *et al.* [5] (+); and Stier and Barnett [34] (□). The cross section for capture into the 1*s* state of the projectile is shown by the short-dashed line.

would be different. This is presented in Fig. 12 where we report our theoretical and experimental results for the case of H^+ colliding with O_2. The long dashed line is the result of Eq. (8) while the solid line is the result of Eq. (7). For completeness, we also compare with the previous experimental measurements of Lindsay *et al.* [3], Stier and Barnett [34], Stebbings *et al.* [5], and Koopman [13]. The uncertainties associated with the data of Lindsay *et al.* [3] are ±6–11% and those with the data of Stier and Barnett [34] are ±5–10%. In both cases, the larger uncertainty applies to the lower energy data. The uncertainty in the data of Koopman is ±15%. The high energy measurements of Rudd *et al.* [35] (not shown) are consistent with the other experiments but are subject to significantly greater uncertainty. It is also worth noting that the data of Stebbings *et al.* and that of Koopman *et al.* [13] are normalized to the absolute measurements of Stier and Barnett [34]. Our results agree with the experimental data at energies above 1.0 keV for both of our descriptions. For the lower projectile energies, we see a dip in the total charge exchange cross section for the impact parameter description of the cross section. From the results in Figs. 8–10, we attribute this to the narrow region where the *p* orbitals affect the charge exchange.

At energies below 1 keV, there is discrepancy between our calculations and the experimental data. As mentioned earlier, a multiconfigurational treatment of the electronic structure for O_2 is required for a better description of low energy collisions. Work has already begun to adapt END in this direction and it is hoped that the improved version will ultimately resolve this discrepancy.

In the same figure we show the total electron capture by the projectile into the 1*s* state, which is obtained by projecting the final electronic wave function on the 1*s* state of the hydrogen atom. It is obvious that the projectile leaves the collision with a high probability of finding an electron in the 1*s* state at low projectile energies. For higher projectile energies, high energy levels start to be populated, and the ionization channel starts to open.

V. CONCLUSIONS

Characterization of the dynamics of the collision of protons with molecular oxygen is carried out experimentally and theoretically. For the theoretical analysis we use the electron-nuclear dynamics approach to approximate the time-dependent Schrödinger equation. We show that by using the Schiff approximation to include quantum interference effects in the description of the direct differential cross section, and by using the deflection function obtained through the dynamical END formalism, good agreement is obtained between theory and experiment. Good general agreement is also obtained for the differential electron transfer cross section, particularly at high projectile energies where the single collision approach holds. A diffraction slit effect, which is target orientation dependent, is found in the differential scattering cross section and a theoretical explanation is given.

ACKNOWLEDGMENTS

This work was supported partially by NSF (Grant No. ATM-0108734 to B.G.L.), ONR (Grants No. N0014-97-1-0261 to Y.O. and E.D. and No. N0014-96-1-00707 to J.R.S.), and by an IBM SUR grant. This support is gratefully acknowledged.

[1] R. Cabrera-Trujillo, Y. Öhrn, E. Deumens, J. R. Sabin, and B. G. Lindsay, Phys. Rev. A **66**, 042712 (2003).
[2] R. Cabrera-Trujillo, Y. Öhrn, E. Deumens, and J. R. Sabin, J. Chem. Phys. **116**, 2783 (2002).
[3] B. G. Lindsay, D. R. Sieglaff, D. A. Schafer, C. L. Hakes, K. A. Smith, and R. F. Stebbings, Phys. Rev. A **53**, 212 (1996).
[4] J. S. Nisbet, Planet. Space Sci. **27**, 243 (1979).
[5] R. F. Stebbings, A. C. Smith, and H. Ehrhardt, J. Geophys. Res. **69**, 2349 (1964).
[6] B. Hamre, J. P. Hansen, and L. Kocbach, J. Phys. B **32**, L127 (1999).
[7] P. C. Stancil, D. R. Schultz, M. Kimura, J. P. Gu, G. Hirsch, and R. J. Buenker, Astron. Astrophys., Suppl. Ser. **140**, 225 (1999).
[8] W. R. Thompson, M. B. Shah, and H. B. Gilbody, J. Phys. B **29**, 725 (1996).
[9] D. Belkic, Phys. Rev. A **37**, 55 (1988).
[10] R. A. Mapleton, Phys. Rev. **130**, 1829 (1963).

[11] R. S. Gao, L. K. Johnson, C. L. Hakes, K. A. Smith, and R. F. Stebbings, Phys. Rev. A **41**, 5929 (1990).
[12] H. H. Fleischmann, R. A. Young, and J. W. McGowan, Phys. Rev. **153**, 19 (1967).
[13] D. W. Koopman, Phys. Rev. **166**, 57 (1968).
[14] E. Deumens, A. Diz, R. Longo, and Y. Öhrn, Rev. Mod. Phys. **66**, 917 (1994).
[15] Y. Öhrn, E. Deumens, A. Diz, R. Longo, J. Oreiro, and H. Taylor, *Time-Dependent Quantum Molecular Dynamics* (Plenum, New York, 1992).
[16] E. Deumens and Y. Öhrn, J. Phys. Chem. **92**, 3181 (1988).
[17] E. Deumens, A. Diz, H. Taylor, and Y. Öhrn, J. Chem. Phys. **96**, 6820 (1992).
[18] J. B. Delos, Rev. Mod. Phys. **53**, 287 (1981).
[19] D. J. Thouless, Nucl. Phys. **21**, 225 (1960).
[20] J. R. Klauder and B. S. Skagerstman, *Coherent States, Applications in Physics and Mathematical Physics* (World Scientific, Singapore, 1985).
[21] R. S. Mulliken, J. Chem. Phys. **36**, 3428 (1962).
[22] R. Cabrera-Trujillo, J. R. Sabin, E. Deumens, and Y. Öhrn, in *Application of Accelerators in Research and Industry*, edited by J. L. Duggan and I. Lon Morgan, AIP Conf. Proc. No. 576, (AIP, Melville, NY, 2001), p. 3.
[23] E. Deumens, T. Helgaker, A. Diz, H. Taylor, J. Oreiro, B. Mogensen, J. A. Morales, M. C. Neto, R. Cabrera-Trujillo, and D. Jacquemin, ENDyne version 2.8 software for electron nuclear dynamics, Quantum Theory Project, University of Florida, Gainesville, FL 32611-8435, 2000.
[24] R. Cabrera-Trujillo, J. R. Sabin, Y. Öhrn, and E. Deumens, Phys. Rev. A **61**, 032719 (2000).
[25] L. I. Schiff, Phys. Rev. **103**, 443 (1956).
[26] D. Jacquemin, J. A. Morales, E. Deumens, and Y. Öhrn, J. Chem. Phys. **107**, 6146 (1997).
[27] T. H. Dunning, J. Chem. Phys. **90**, 1007 (1989).
[28] D. E. Woon and T. H. Dunning, J. Chem. Phys. **100**, 2975 (1994).
[29] L. K. Johnson, R. S. Gao, C. L. Hakes, K. A. Smith, and R. F. Stebbings, Phys. Rev. A **40**, 4920 (1989).
[30] R. S. Gao, P. S. Gibner, J. H. Newman, K. A. Smith, and R. F. Stebbings, Rev. Sci. Instrum. **55**, 1756 (1984).
[31] Baratron model 390HA manufactured by MKS, Pressure Measurement & Control Products, Six Shattuck Road, Andover, MA 01810, USA.
[32] J. H. Newman, K. A. Smith, R. F. Stebbings, and Y. S. Chen, J. Geophys. Res., [Space Phys.] **90**, 11045 (1985).
[33] N. F. Mott and H. S. W. Massey, *The Theory of Atomic Collisions* (Clarendon Press, Oxford, 1965).
[34] P. M. Stier and C. F. Barnett, Phys. Rev. **103**, 896 (1956).
[35] M. E. Rudd, R. D. DuBois, L. H. Toburen, C. A. Ratcliffe, and T. V. Goffe, Phys. Rev. A **28**, 3244 (1983).